RSC Advances

PAPER

View Article Online
View Journal | View Issue

Cite this: *RSC Adv.*, 2026, **16**, 14458

Biochar-capped iron oxide nanocomposites prepared by ultrasonic method as nanophotocatalysts for the degradation of organic dyes using response surface methodology

Thandi B. Mbuyazi and Peter A. Ajibade *

Iron oxide nanocomposites (Fe_3O_4@BC–**1**, Fe_3O_4@BC–**2**, and Fe_3O_4@BC–**3**) were synthesized *via* an ultrasound-assisted method at 5, 10, and 15 min to investigate their morphological, optical, and photocatalytic properties. Powder X-ray diffraction (P-XRD) analysis confirmed the formation of Fe_3O_4 with a cubic spinel structure. TEM analysis revealed that Fe_3O_4@BC–**1** exhibited irregular rod- and plate-like structures with a particle size of 6.4 nm, Fe_3O_4@BC–**2** displayed square-shaped particles with a mean size of 8.3 nm, and Fe_3O_4@BC–**3** consisted of agglomerated particles with a size of 9.8 nm. Optical analysis showed a redshift in absorption peaks from 400 nm (2.36 eV) for Fe_3O_4@BC–**1** to 417 nm (2.28 eV) for Fe_3O_4@BC–**2**, and 418 nm (2.32 eV) for Fe_3O_4@BC–**3**. The nanocomposites were evaluated as photocatalysts against Congo red (CR) and crystal violet (CV) using response surface methodology. Fe_3O_4@BC–**3** exhibited the highest photocatalytic degradation efficiency of 99.86% of CR under optimal conditions (120 min, 3 mg, 15 ppm, pH 3) and Fe_3O_4@BC–**2** achieved 99.28% degradation of CV under 90 min, 8 mg, and pH 8 for 5 ppm CV. Reactive species analysis confirmed hydroxyl ($^{\bullet}OH$) and superoxide radicals ($^{\bullet}O_2^-$) as the dominant contributors to the dye's degradation.

Received 16th December 2025
Accepted 8th March 2026

DOI: 10.1039/d5ra09734g

rsc.li/rsc-advances

1. Introduction

The continuous discharge of significant quantities of synthetic dyes into the aquatic ecosystem poses severe environmental and public health challenges.[1,2] Most of the organic dyes used in textiles, paper, and printing industries are major public health concerns because they are toxic, non-biodegradable and a major source of environmental pollutants.[3–5] Conventional wastewater treatment techniques often fail to effectively remove these dyes, which necessitates the development of more efficient and sustainable approaches.[6,7] Among the advanced methodologies, photocatalysis could completely mineralize organic dyes to carbon dioxide and water under mild conditions and does not rely on mass transfer.[8] Photocatalysis effectiveness depends significantly on the choice of the photocatalyst, which should ideally exhibit high stability, be an efficient light absorber, and have strong interactions with pollutants.[9,10] In recent years, biochar-capped iron oxide nanocomposites have received tremendous attention as a multifunctional material for environmental remediation.[11,12] The combination of biochar, a carbon-rich material derived from biomass, with iron oxide nanoparticles enhances adsorption capacity, promotes electron transfer, and minimizes the aggregation of nanoparticles, thereby improving photocatalytic performance.[13–15] However, the optimization of the experimental parameters governing photocatalytic degradation remains a critical step to maximize efficiency and practical applicability.

Statistical optimization methods, such as response surface methodology (RSM), provide a systematic approach for evaluating the complex interactions between multiple variables and determining their optimal levels.[16] The Box–Behnken design (BBD), a widely used RSM technique, offers an efficient framework for exploring these interactions while minimizing the number of experimental runs required.[17–19] By employing BBD, researchers can identify the most influential factors and their interactions, thus streamlining the optimization process. This study aims to utilize the Box–Behnken design to optimize the photocatalytic degradation of crystal violet (CV) and Congo red (CR) using biochar-capped iron oxide nanocomposites prepared using ultrasonic techniques. The specific objectives include evaluating the effects of key operational parameters, such as pH, catalyst dosage, and dye concentration, on the degradation efficiency and determining the optimal conditions for maximum removal of the target dyes. By developing efficient photocatalysts for dye removal and utilizing biochar derived from biomass, this work contributes to SDG 6 (Clean Water and Sanitation) which aims to improve water quality through pollution reduction, and to SDG 12 (Responsible Consumption and Production) by promoting the reuse of biomass waste.

School of Chemistry and Physics, University of KwaZulu-Natal, Private Bag X01, Scottsville, Pietermaritzburg, 3209, South Africa. E-mail: ajibadep@ukzn.ac.za

2. Materials and methods

2.1 Reagents and materials

All chemicals used in different experimental steps, such as $FeCl_2 \cdot H_2O$, NaOH, ethanol, Congo red, crystal violet, HCl, methanol, acrylamide, silver nitrate, and formic acid, were obtained from Sigma-Aldrich and were used without any purification. *Portulacaria afra* biochar was prepared as reported.[20] All reagents and nanomaterials prepared were handled with appropriate personal protective equipment in a fume hood, and waste was disposed of according to institutional safety guidelines to minimize exposure and environmental release.

2.2 Synthesis of iron oxide nanocomposites

The nanocomposites were synthesized using a one-salt method.[21] 0.5 g of $FeCl_2 \cdot H_2O$ was dissolved in 100 mL of distilled water and stirred magnetically for 10 minutes. Subsequently, 0.5 g of biochar was added to the solution, followed by the addition of 10 mL of 3 M NaOH. The mixture was then sonicated for 5 minutes using a QSONICA Q700 ultrasonic processor (700 W, 20 kHz) at 50% amplitude. The resulting precipitate was collected, thoroughly washed four times by centrifugation at 5000 rpm for 15 minutes with water and ethanol. The supernatant was discarded, and the resulting black solid was dried in an oven for 6 h. To study the effect of ultrasonic irradiation time on the iron oxide nanocomposites, the experiment was repeated for 10 and 15 minutes.

2.3 Physical characterization

High-resolution transmission electron microscopy (HRTEM) micrographs, selected area electron diffraction (SAED) patterns, and lattice fringes of the nanocomposites were obtained using a JEOL JEM-2100 microscope. Scanning electron microscopy (SEM) and energy-dispersive X-ray spectroscopy (EDX) analyses were carried out using a ZEISS EVO LS15 electron microscope. Powder X-ray diffraction (XRD) patterns were recorded using a Bruker D8 diffractometer equipped with Cu Kα radiation. Photocatalytic experiments were conducted under an OSRAM HQL (MBF-U) 125 W lamp. UV-vis absorbance spectra were measured in the 200–700 nm range using a PerkinElmer Lambda 25 spectrometer.

2.4 Photocatalytic studies

The photocatalytic activity of the Fe_3O_4@BC nanocomposites was evaluated using CR and CV at concentrations ranging from 5 to 25 ppm. 2–12 mg of the nanocomposite was dispersed in 6 mL of the dye solution and sonicated for 30 minutes, followed by stirring in the dark for 60 minutes to achieve adsorption–desorption equilibrium. The mixture was then exposed to irradiation from a 125 W high-pressure mercury vapor lamp (colour temperature 4100 K) for 120 minutes under constant stirring at 2000 rpm. The light was positioned at 15 cm above the 10 mL borosilicate tubes. After irradiation, UV-vis spectra of the solutions were recorded to analyse the photodegradation of the dyes. The pH of the dye solutions was adjusted using 0.1 M HCl or 0.1 M NaOH. The study investigated the influence of key parameters, such as dye concentration, irradiation time, solution pH, and catalyst dosage, on the degradation efficiency using the RSM with a BBD model.

Table 1 Independent variables and their levels

	Levels		
Reaction parameters	High (+1)	Central (0)	Low (−1)
A: Time (min)	120	70	20
B: Catalyst dosage (mg)	12	7	2
C: Dye concentration (ppm)	25	15	5
D: pH	9	6	3

2.5 Optimization of photocatalysis

Box–Behnken design was used to model, optimize and determine the influences of independent variables and their interactions on the photocatalytic degradation of the organic dyes using Design-Expert 13.0.0 software.[22] Four reaction parameters were evaluated as independent variables at three levels as shown in Table 1. These parameters are pH, catalyst dose, dye concentration, and contact time. Tables S2–S4 present the design with experimental values for independent variables, predicted, and experimental degradation efficiency.

The models follow a quadratic polynomial equation structure:

$$Y = \beta_0 + \sum \beta_i X_i + \sum \beta_{ij} X_i X_j + \sum \beta_{ii} X_i^2$$

where Y is degradation efficiency (%), β_0 is the intercept, X_i represents independent variables, β_i denotes the main effects (A, B, C, and D), β_{ij} represents the effects of two variables combined and β_{ii} represents curvature effects.

2.6 Effects of scavengers

The influence of reactive species on the photocatalysis process were evaluated by performing scavenging experiments methanol (MeOH), acrylamide (AC), silver nitrate (SN), and formic acid (FA) were added to the reaction mixture to selectively quench hydroxyl radicals ($^{\bullet}OH$), superoxide radicals ($^{\bullet}O_2^-$), electrons (e^-), and holes (h^+), respectively. The photocatalyst and 5 mL of each scavenger (10 mM concentration) were introduced into the dye solution. The reaction was conducted under visible light irradiation for 120 minutes, and the progress of the degradation process was monitored with UV-vis spectroscopy.

2.7 Photostability studies

The recyclability and photostability of the nanocomposites were evaluated over 6 photocatalytic cycles under the optimized reaction conditions. The photocatalyst was isolated by a magnetic bar after each cycle, rinsed with distilled water and ethanol, then dried in the oven for 2 h at 60 °C.

3. Results and discussion

3.1 Structural and morphological studies

Powder X-ray diffraction patterns of the biochar-capped iron oxide nanoparticles synthesized at different ultrasound durations are presented in Fig. 1. The XRD analysis of biochar (Fig. S1) revealed several peaks indicative of various crystalline phases. Stable carbonaceous material is shown by a broad peak at 20–40°.[23] The peak at 29.44° is attributed to quartz, while the peaks at 28.23° and 41.98° correspond to sylvite.[24] Additionally, the peak at 50.91° closely matched calcite, typical of biochar derived from biomass. The XRD patterns of the nanocomposites prepared at different ultrasound durations confirmed the successful synthesis of the magnetite nanoparticles. Major diffraction peaks were indexed to the cubic spinel structure of Fe_3O_4, corresponding to the JCPDS card no. 00-011-0614.[25,26] The major diffraction planes identified were (111), (220), (311), (222), (400), (511), (440), (442), (533), (622), and (444), which confirm the magnetite crystalline phase of iron oxide. The presence of biochar peaks in all nanocomposites confirms the successful incorporation of biochar within the composite structure. Notably, the Fe_3O_4@BC–**2** composite exhibited fewer biochar peaks compared to Fe_3O_4@BC–**1** and Fe_3O_4@BC–**3**, resulting in more well-defined magnetite peaks. This suggests that the sonication duration of 10 minutes facilitated better dispersion and integration of the iron oxide phase within the biochar matrix, reducing the dominance of biochar peaks.

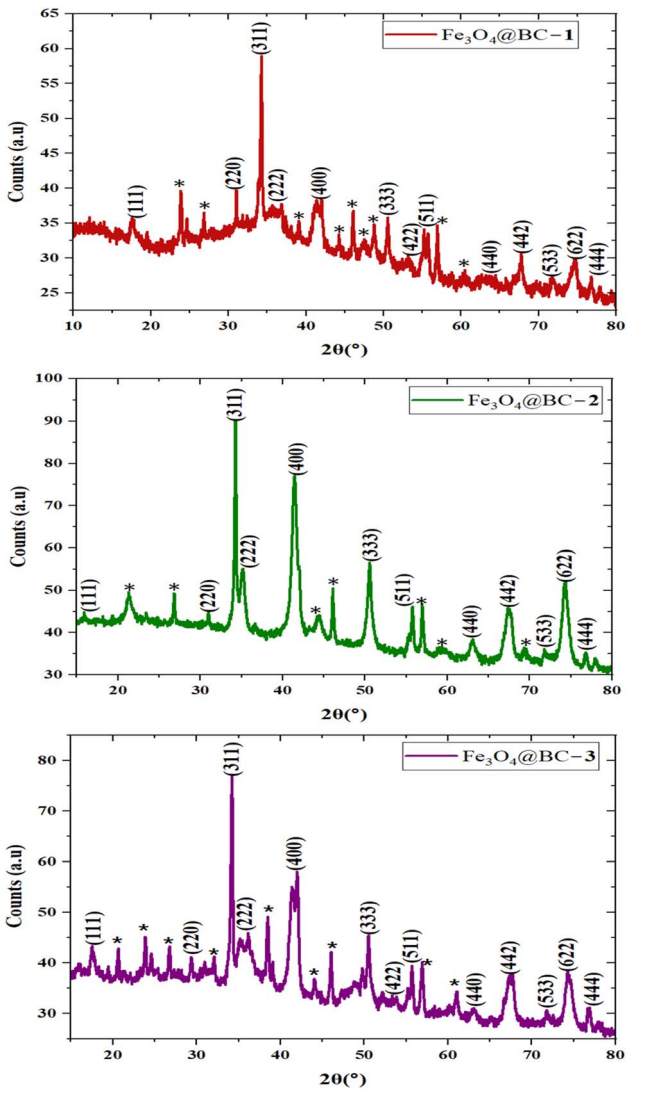

Fig. 1 P-XRD patterns of magnetite nanocomposites Fe_3O_4@BC–**1**, Fe_3O_4@BC–**2** and Fe_3O_4@BC–**3** synthesized at 5 min, 10 min and 15 min, respectively. * Biochar peaks.

The HRTEM micrographs and particle size distribution histograms (Fig. 2) of the biochar-capped iron oxide nanocomposites synthesized using ultrasound treatment at (5 min, 10 min, and 15 min), are labelled as Fe_3O_4@BC–**1**, Fe_3O_4@BC–**2**, and Fe_3O_4@BC–**3**, respectively. Fe_3O_4@BC–**1** exhibits irregular morphology with some rod particles with an average diameter of 6.4 nm. This small particle size can be attributed to the high-intensity cavitation effects during the initial stages of ultrasound exposure, which promote rapid nucleation and inhibit particle growth.[27] Fe_3O_4@BC–**2** micrograph reveals more defined square and irregularly shaped particles with reduced aggregation compared to Fe_3O_4@BC–**1**. The particles are more uniformly dispersed with an average diameter of 8.3 nm. Fe_3O_4@BC–**3** nanocomposite shows square, rectangular, and quasi-spherical particles with increased aggregation and larger particles with an average size of 9.8 nm. Some areas exhibit denser nanocomposite packing, possibly due to prolonged ultrasound exposure facilitating growth and coalescence.[28] Fig. 2(b) shows lattice fringes of the nanocomposites where Fe_3O_4@BC–**1** and Fe_3O_4@BC–**3** show five distinct *d*-spaces corresponding to (220), (222), (311), (400), and (440) planes of magnetite.[29–31] In contrast, Fe_3O_4@BC–**2** reveals two interplanar spaces of 0.479 and 0.248 nm, which correlate to (111) and (222) planes of magnetite.[32,33] The SAED patterns in Fig. 2(c) show rings with bright spots indicating the polycrystallinity of the nanocomposites. The ultrasound synthesis method used in this study provides a rapid and energy-efficient route for preparing iron oxide nanocomposites with diverse morphologies. However, despite these advantages, scaling up ultrasonic synthesis remains challenging as the cavitation effect that drives nanoparticle formation is highly localized and difficult to reproduce uniformly in larger volumes.[34]

Fe_3O_4@BC–**1** SEM image in Fig. S3 shows a biochar-capped iron oxide nanocomposite with a heterogeneous morphology. Rough and porous clusters of iron oxide nanocomposite with a range of morphologies, including irregular, granular, and some more defined polygonal shapes. Fe_3O_4@BC–**2** SEM image exhibits densely packed granular particles with a rough texture. SEM image of a Fe_3O_4@BC–**3** nanocomposite displays a smooth morphology with multiple layers of rod-like particles and smaller granular particles. The corresponding EDS spectra show a clear trend in surface elemental composition. Fe_3O_4@BC–**1** has the lowest Fe content of 2.04%, with a dominant carbon content of 54.59% and 35.12% of oxygen. Fe_3O_4@BC–**2** shows a slight increase in Fe to 4.93%, with a high carbon content of 59.13% and reduced oxygen (27.83%). Fe_3O_4@BC–**3** exhibits a drastically high Fe on the surface (55.34%), with a significantly reduced carbon (18.16%) and oxygen (10.19%). The minor elements detected are typical ash residues from biochar precursor and show no trend with

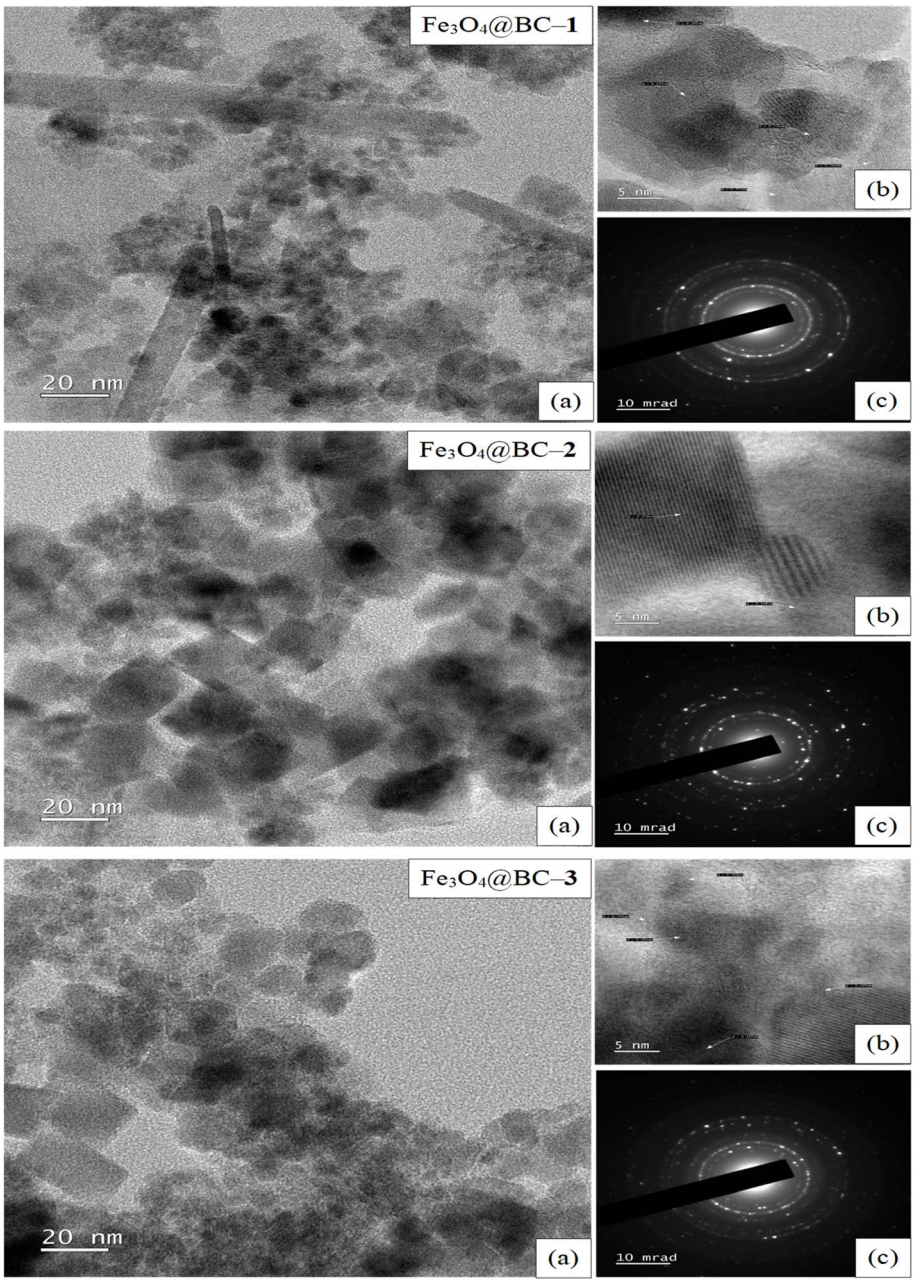

Fig. 2 HRTEM images (a), lattice fringes (b) and SAED patterns (c) of biochar-capped iron oxide nanocomposites.

sonication time. The results show that short ultrasonic duration provides insufficient incorporation of iron oxide nanoparticles into biochar, whereas prolonged ultrasonication induces agglomeration and a Fe-rich surface due to clustering.

The FTIR spectra of magnetite nanoparticles, biochar derived from *Portulacaria afra* leaves, and Fe_3O_4@BC nanocomposites before and after photocatalysis are presented in Fig. S4. The bare Fe_3O_4 nanoparticles exhibited a prominent absorption band around 550 cm^{-1}, corresponding to the Fe–O stretching vibration, which confirms the formation of the magnetite spinel structure.[35] The broad band around 3420 cm^{-1} is assigned to the O–H stretching vibrations of surface hydroxyl groups and adsorbed water, while the peak near 1610 cm^{-1} arises from the bending vibration of H–O–H.[36] The biochar displayed several characteristic peaks associated with oxygenated and aromatic functionalities. The broad O–H stretching band near 3400 cm^{-1}, the C=O stretching vibration at 1600 cm^{-1}, and peaks at 1450 cm^{-1} and 760 cm^{-1}, corresponding to C=C stretching and aromatic ring vibrations,[37] respectively, indicate the presence of hydroxyl, carbonyl, and aromatic groups on the biochar.

The FTIR spectrum of the Fe_3O_4@BC nanocomposites exhibited peaks of both magnetite and biochar, confirming successful integration of the two materials. The biochar-derived peaks at 1450 cm^{-1} and 760 cm^{-1} were also observed in the composite but showed a slight shift of approximately 15 cm^{-1}, indicating strong interfacial interactions between the Fe_3O_4 nanoparticles and the

biochar matrix.[38] The FTIR spectra of the post-catalysis nanocomposites retained the characteristic bands of both magnetite and biochar, suggesting that the core structure of the composite remained stable after the photocatalytic reaction.

3.2 Optical properties

The optical properties of iron oxide nanocomposites, particularly their light absorption characteristics, are crucial for applications in photocatalysis.[39,40] In this study, the absorption wavelengths of the nanocomposites synthesized using an ultrasound method at different time intervals were evaluated and presented in Fig. S5(a). Optical bandgap energies were estimated using Tauc plots in Fig. 5(b), obtained by plotting $(\alpha h\nu)^2$ *versus* $(h\nu)$ for the direct allowed transition.[41] Fe_3O_4@BC–**1** exhibited an absorption peak at 400 nm, corresponding to a bandgap energy of 2.36 eV. The smaller average particle size of 6.4 nm contributes to a wider bandgap, consistent with the quantum confinement effect.[42] For Fe_3O_4@BC–**2** the absorption peak shifted to 417 nm, corresponding to a lower bandgap energy of 2.28 eV. This redshift in the absorption wavelength can be attributed to the increase in average particle size. Larger particles exhibit reduced quantum confinement effects, resulting in a narrowing of the bandgap and absorption of longer wavelengths.[43] For Fe_3O_4@BC–**3**, the absorption peak was observed at 418 nm, with a bandgap energy of 2.32 eV. The marginal redshift relative to the Fe_3O_4@BC–**2** suggests that the shift in morphology may influence electronic properties, further contributing to the observed optical changes.[44] The results reveal that the ultrasonic irradiation time significantly influences the optical properties of the nanocomposites, which may be due to changes in their size and morphology.

4. Analysis of the Box–Behnken design

4.1 Statistical analysis and model validation

The RSM models for CR and CV degradation show the effect of time (A), catalyst dosage (B), dye concentration (C), and pH (D), and their interactions on the degradation efficiency using three iron oxide nanocomposites (Fe_3O_4@BC) photocatalysts. Fig. S6 shows predicted *vs.* actual plots for the degradation efficiency of crystal violet and Congo red using iron oxide nanocomposites. All plots show data points closely aligned and correlate between predicted and actual values. The BBD model effectively predicts degradation efficiency for all three iron oxide nanocomposites, with minimal deviation from actual values.

The perturbation plots in Fig. S7 illustrate the sensitivity of photodegradation efficiency to different independent variables for iron oxide nanocomposites in the degradation of CV and CR. A comparative analysis of the two dyes shows that the photocatalyst dosage consistently enhances CV degradation. In contrast, photocatalyst dosage exhibits different effects for CR. For Fe_3O_4@BC–**1** and Fe_3O_4@BC–**2**, increasing catalyst dosage positively affects degradation efficiency. However, for Fe_3O_4@BC–**3**, catalyst dosage follows a parabolic trend, indicating that excessive catalyst concentration may reduce the degradation efficiency. pH exerts a strong hindrance to the photodegradation of both dyes.

The ANOVA statistical parameters for the fitted quadratic model of CR and CV dye degradation are presented in Tables S5–S10. The results confirmed that the overall model was highly significant ($p < 0.0001$) for all catalysts and both dyes,[45] indicating that the selected variables strongly influenced degradation efficiency. For CR, reaction time, catalyst dosage, dye concentration, and pH were consistently significant ($p < 0.0001$), demonstrating their critical roles in the reaction. Interaction effects varied across catalysts, while AB, AD, and BC were significant in multiple cases, AC and CD were generally non-significant. Quadratic effects were particularly pronounced for B^2 and D^2, suggesting a nonlinear relationship requiring optimization for maximum efficiency. For CV, all primary factors (A, B, C, and D) remained highly significant ($p < 0.0001$) for Fe_3O_4@BC–**1** and Fe_3O_4@BC–**3**, confirming their strong influence on dye degradation. However, for Fe_3O_4@BC–**2**, reaction time and catalyst dosage were not significant individually, nevertheless, their interaction effects (AB, AC) played crucial roles. Significant two-factor interactions were observed for AB, AD, and BC, highlighting the importance of factor interplay. Quadratic terms were mostly significant ($p < 0.05$), indicating the necessity of optimizing each variable to achieve the highest photocatalytic efficiency.[46] These results suggest that the degradation of both dyes is highly dependent on reaction conditions, with nonlinearity and interaction effects playing substantial roles.

4.2 3D-Surface interactive plots analysis

The catalytic degradation of CR and CV using iron oxide nanocomposites was studied using the Box–Behnken design. The study evaluates the effects of catalyst dosage, dye concentration, and pH on degradation efficiency over 120 minutes. The catalyst dosage is a critical parameter in determining the photocatalytic degradation efficiency of organic dyes, as it directly influences the number of available active sites and the photon utilization in the reaction.[47,48] For all catalysts, increasing the dosage initially improved degradation efficiency due to a higher number of active sites available for the reaction and by generating more reactive species. However, beyond an optimal dosage, the efficiency decreased. Fe_3O_4@BC–**1** showed a continuous increase in efficiency with increasing catalyst dosage (Fig. 3(a)) due to the relatively smaller particle size and better dispersion. Fe_3O_4@BC–**2** in Fig. 4(a) reached maximum efficiency at 8.5 mg (81.53%) but decreased beyond this point, due to particle agglomeration, which reduces effective surface area exposed to dye molecules and visible light, limits mass transfer, and decreases accessible active sites.[49] Fe_3O_4@BC–**3** in Fig. 5(a) exhibited a similar trend, with maximum efficiency at 8 mg (73.97%), decreasing to 57.60% at 12 mg due to aggregation. Excessive catalyst loading can increase solution turbidity, leading to light scattering and reduced photon penetration, thereby lowering the generation of photogenerated charge carriers.[50] These competing effects indicate that optimizing catalyst dosage is crucial for achieving a balance between maximizing available active sites and minimizing aggregation while maintaining high degradation efficiency.

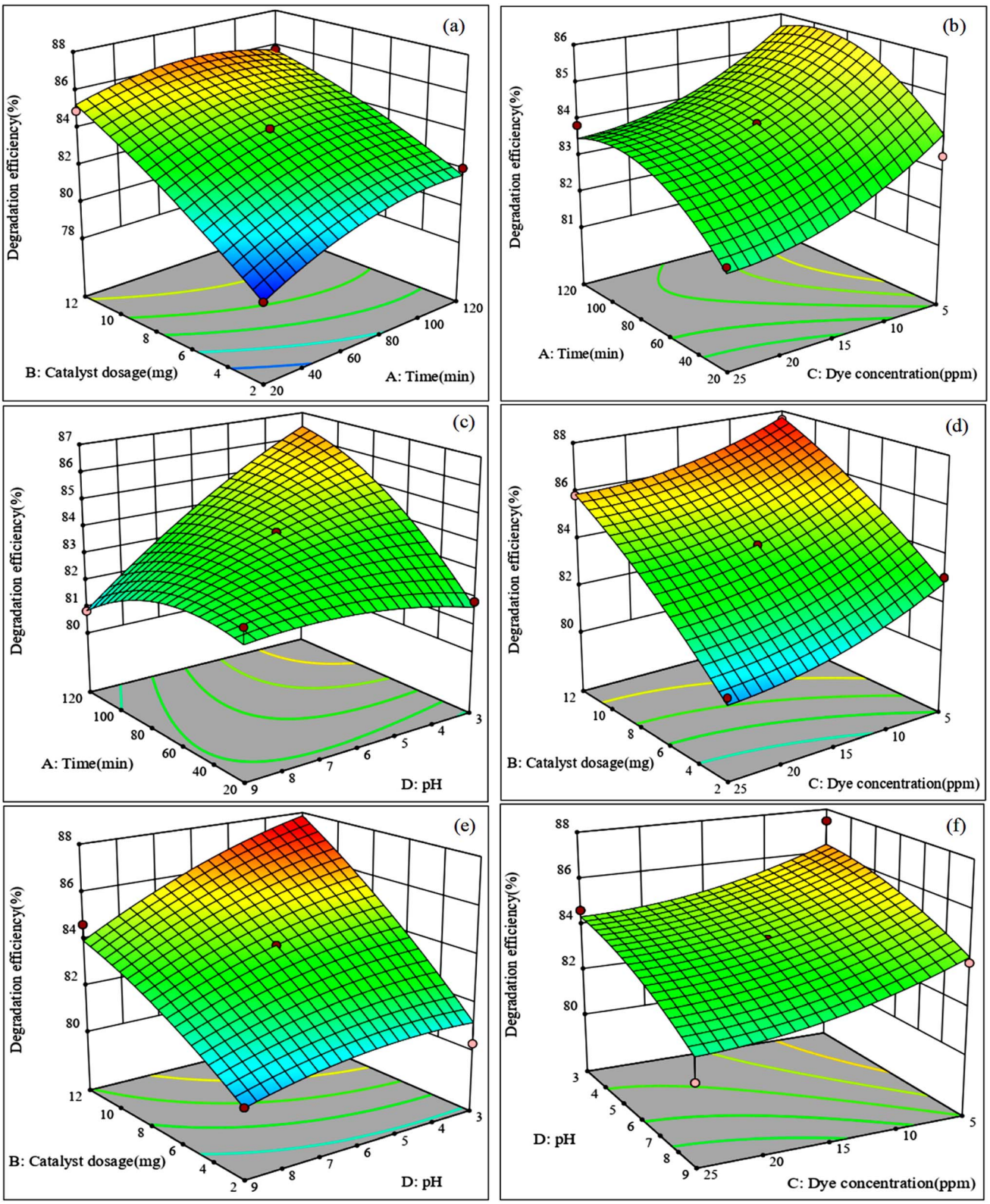

Fig. 3 Degradation of CR by Fe_3O_4@BC–**1** 3D response surface plot of (a) time *vs.* catalyst dosage, (b) time *vs.* dye concentration, (c) time *vs.* pH, (d) catalyst dosage *vs.* dye concentration, (e) catalyst dosage *vs.* pH and (f) dye concentration *vs.* pH.

The initial dye concentration played a significant role in the degradation efficiency. Fe_3O_4@BC–**1** exhibited only a slight decrease in efficiency with increase in CR concentration from 5 ppm (86.67%) to 25 ppm (85.84%), suggesting that the catalyst can be used in a wide range of dye concentrations (Fig. 3(b)). Fe_3O_4@BC–**2** in Fig. 4(b) showed a more pronounced drop in

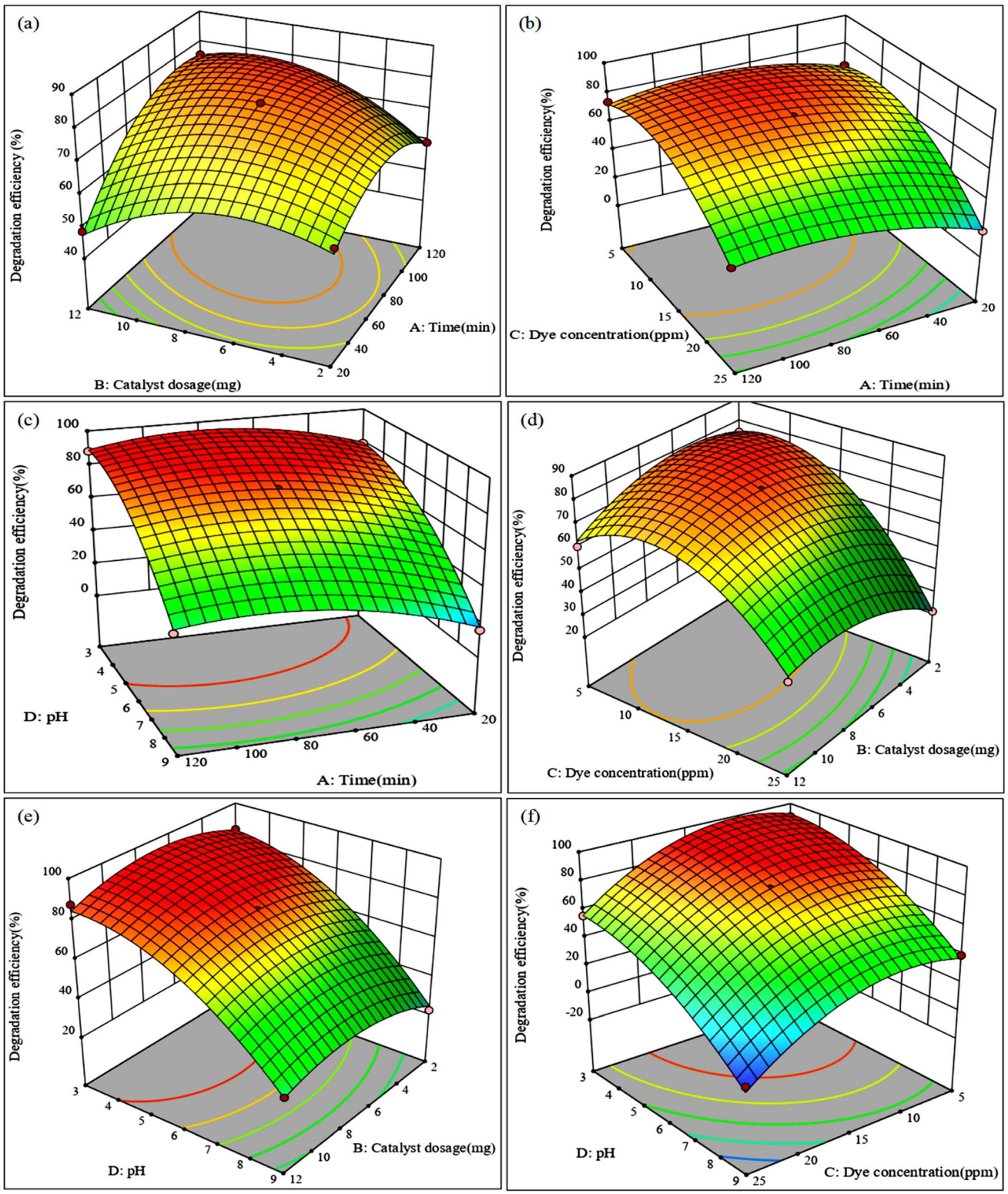

Fig. 4 Degradation of CR by Fe_3O_4@BC–2 3D response surface plots of (a) time *vs.* catalyst dosage, (b) time *vs.* dye concentration, (c) time *vs.* pH, (d) catalyst dosage *vs.* dye concentration, (e) catalyst dosage *vs.* pH and (f) dye concentration *vs.* pH.

efficiency from 79.17% at 15 ppm to 40.54% at 25 ppm, suggesting that higher dye concentration saturates catalyst active sites, reducing performance.[51] Fig. 5(b) shows that Fe_3O_4@BC–**3** achieved 97.07% degradation at 5 ppm but decreased significantly to 48.97% at 25 ppm, implying that excessive dye concentration limits active site availability and radical formation.[52] These trends indicate that while Fe_3O_4@BC–**1** maintains efficiency under higher dye loads, Fe_3O_4@BC–**2** and

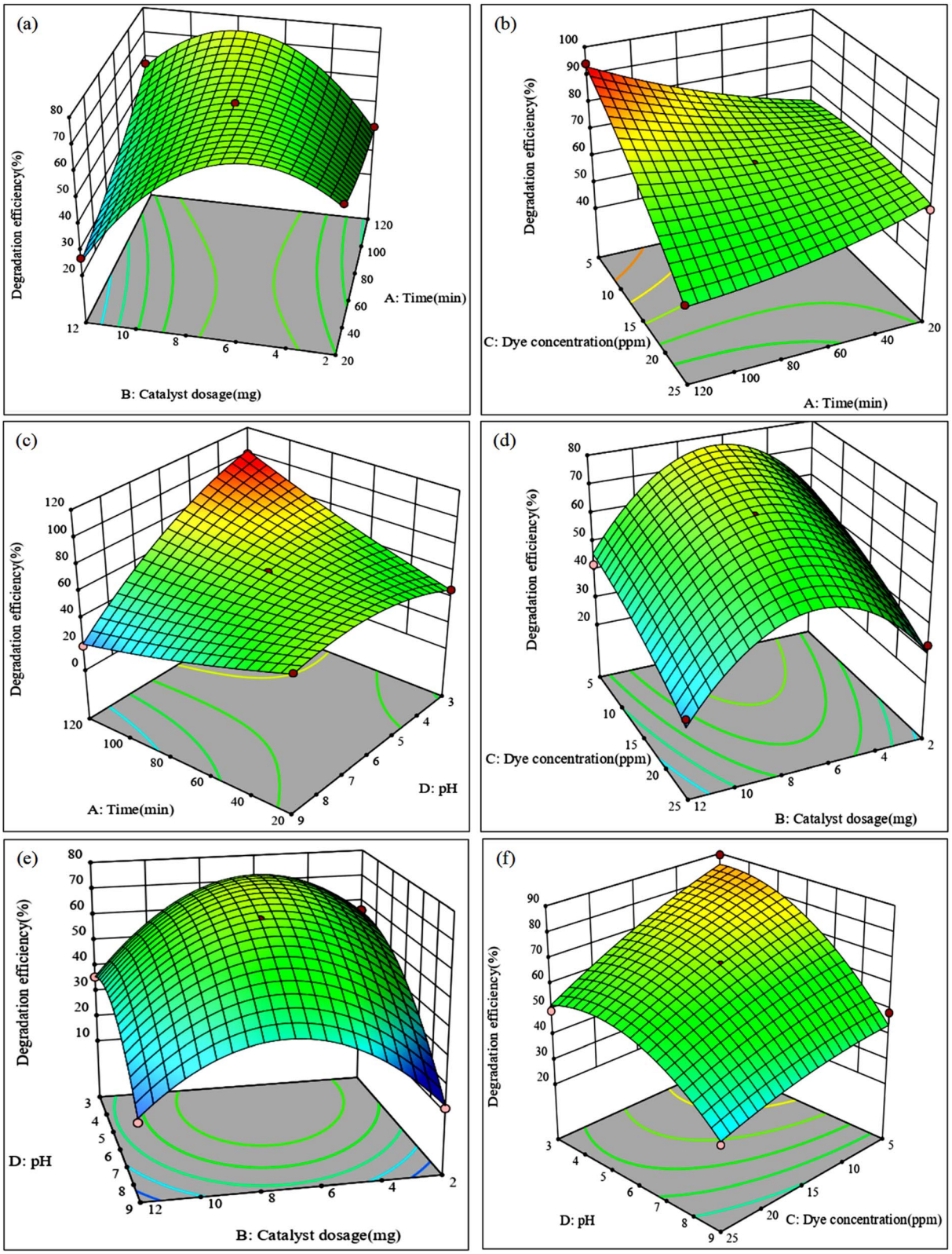

Fig. 5 Degradation of CR by Fe_3O_4@BC–3 3D response surface plots of (a) time *vs.* catalyst dosage, (b) time *vs.* dye concentration, (c) time *vs.* pH, (d) catalyst dosage *vs.* dye concentration, (e) catalyst dosage *vs.* pH and (f) dye concentration *vs.* pH.

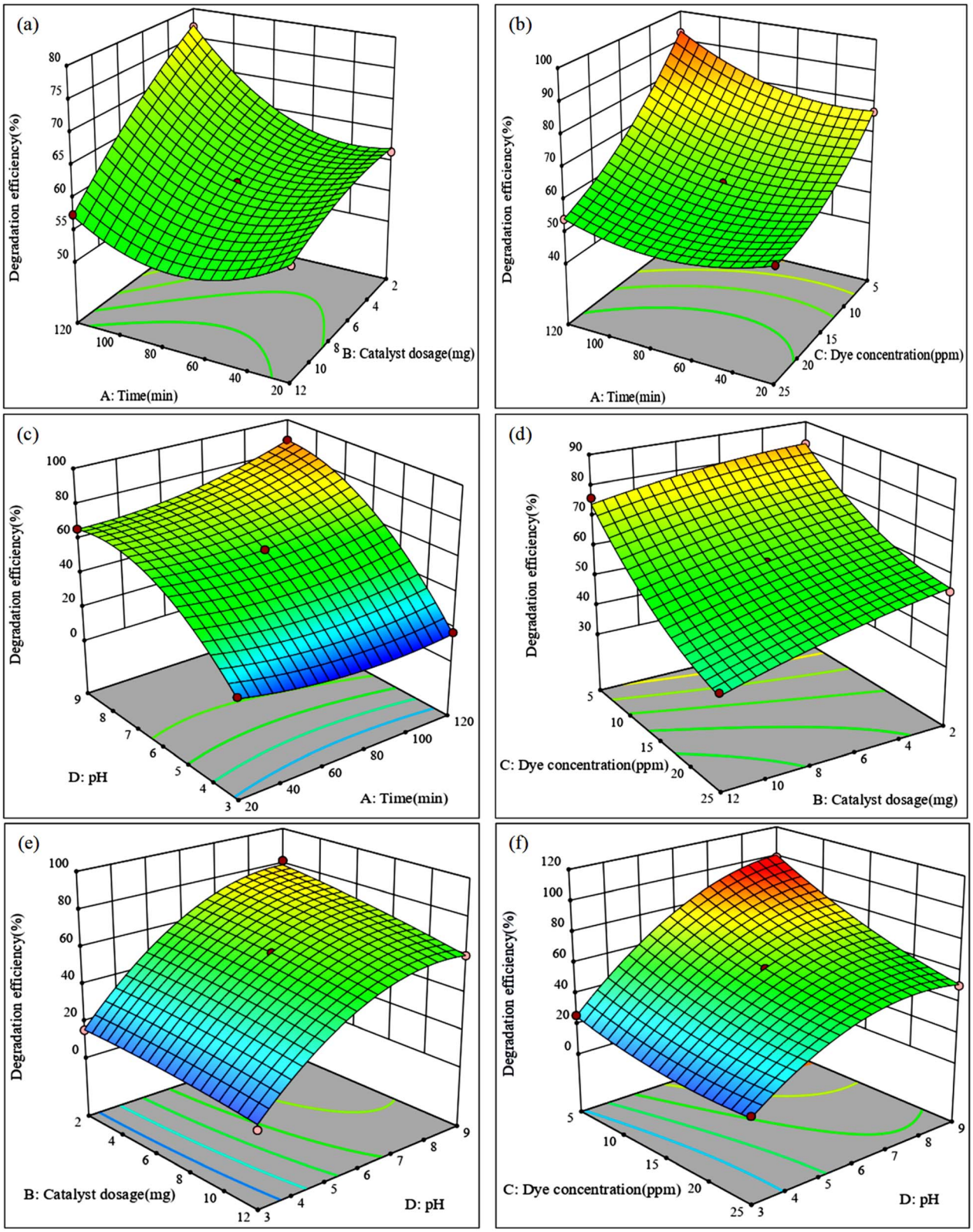

Fig. 6 Degradation of CV by Fe_3O_4@BC–**1** 3D response surface plot of (a) time *vs.* catalyst dosage, (b) time *vs.* dye concentration, (c) time *vs.* pH, (d) catalyst dosage *vs.* dye concentration, (e) catalyst dosage *vs.* pH and (f) dye concentration *vs.* pH.

Fe_3O_4@BC–**3** undergo reduced performance due to competitive adsorption effects.

Acidic conditions consistently favoured higher degradation efficiencies across all catalysts, while alkaline conditions led to reduced performance. Fe_3O_4@BC–**1** in Fig. 3(c) shows only a small decrease from 86.40% at pH 3 to 80.95% at pH 9. Fig. 4(c) shows that Fe_3O_4@BC–**2** shows a drastic reduction, with efficiency dropping from 88.09% at pH 3 to 35.13% at pH 9. Fe_3O_4@BC–**3** has the most drastic decrease in efficiency from 99.98% at pH 3 to 19.09% at pH 9 (Fig. 5(c)).

These results suggest that surface charge interactions play a crucial role in degradation. At low pH, the catalysts acquire a positive charge, which enhances the electrostatic attraction with anionic CR molecules.[53] The catalytic activity of Fe_3O_4@BC–**1** remained high across a range of dye concentrations (Fig. 3(d)). The highest efficiency of 86.67% was obtained at 5 ppm dye concentration using 12 mg of catalyst, with only a slight decrease to 85.84% at 25 ppm dye concentration. The high degradation efficiency is attributed to the small particle size, which increases the surface area and provides more active sites for dye–catalyst interactions.[54] Conversely, Fe_3O_4@BC–**2** and Fe_3O_4@BC–**3** demonstrated pronounced sensitivity to changes in both catalyst dosage and dye concentration, with reduced efficiency observed at high catalyst dosage and dye concentration.

For the combined effects of catalyst dosage and pH, Fe_3O_4@BC–**1** exhibited the highest degradation efficiency, achieving 87.82% at pH 3 with 12 mg of catalyst and maintaining a relatively high efficiency of 83.95% at pH 9 (Fig. 3(e)). However, Fe_3O_4@BC–**2** in Fig. 4(e) and Fe_3O_4@BC–**3** in Fig. 5(e) showed stronger pH dependence, performing significantly better in acidic conditions at their optimal catalyst dosages. For the combined effects of dye concentration and pH, Fe_3O_4@BC–**1** exhibited the highest efficiency of 87.82% at pH 3 using 12 mg of catalyst, with a slight decrease to 83.95% at pH 9 (Fig. 3(f)). This suggests that Fe_3O_4@BC–**1** remains effective across a wide pH range, potentially due to its stable surface chemistry and reactive species generation capacity.

In contrast, Fe_3O_4@BC–**2** in Fig. 4(f) and Fe_3O_4@BC–**3** in Fig. 5(f) exhibited strong pH and concentration dependence, with significantly lower efficiency under alkaline conditions and at high dye concentration. The catalyst dosage significantly influenced the degradation efficiency of CV, with an optimal range observed for each catalyst. For Fe_3O_4@BC–**1** in Fig. 6(a), degradation efficiency increased with catalyst dosage up to 2 mg (76.95%) but decreased at higher dosages (57.48% at 12 mg). This decrease in efficiency is attributed to catalyst aggregation at higher dosages, which reduces the effective surface area and active sites.[55] In contrast, Fe_3O_4@BC–**2** in Fig. 7(a) showed a peak efficiency at 7 mg (73.21%), followed by a decrease at 12 mg (64.51%), due to aggregation effects. However, Fe_3O_4@BC–**3** in Fig. 8(a) displayed a consistent increase in degradation efficiency with increase in catalyst dosage, achieving 99.58% efficiency at 12 mg, indicating that higher dosages contribute positively to degradation for this catalyst.[56] These results suggest the importance of optimizing catalyst dosage to balance surface area availability and aggregation effects.

Dye concentration played a crucial role in determining the photocatalytic activity of the nanocomposites. Fig. 6(b) shows that Fe_3O_4@BC–**1** degraded 97.72% of 5 ppm dye after 120 min, but efficiency dropped to 54.09% at 25 ppm, indicating that high dye concentrations saturate active sites and hinder degradation.[57] Fe_3O_4@BC–**2** showed a similar trend in Fig. 7(b), achieving 92.04% efficiency at 5 ppm but dropping to 55.64% at 25 ppm, suggesting that excess dye molecules reduce catalyst activity. Fe_3O_4@BC–**3** in Fig. 8(b) exhibited 90.61% degradation at 5 ppm, with a 16.57% decrease at 25 ppm, further supporting the trend of lower degradation at higher concentrations. These results indicate that an optimal dye concentration is necessary to ensure sufficient catalyst–dye interaction without overloading active sites. The pH of the reaction medium had a substantial impact on dye degradation. For Fe_3O_4@BC–**1** in Fig. 6(c), the highest degradation efficiency was observed at pH 9 (87.74%), while the lowest occurred at pH 3 (17.19%). Fe_3O_4@BC–**2** followed a similar trend, with degradation increasing from 13.73% at pH 3 to 83.14% at pH 8, with a slight drop at pH 9 (79.67%), indicating that pH 8 might be optimal (Fig. 7(c)). Fe_3O_4@BC–**3** in Fig. 8(c) showed its highest degradation efficiency of 86.45% at pH 9, with minimal degradation at pH 3 (20.73%). The improved efficiency at alkaline pH suggests that the catalytic process benefits from enhanced oxidative degradation mechanisms in basic solution.[58] In contrast, acidic conditions (pH 3) may suppress catalytic activity due to electrostatic interactions that hinder dye adsorption. The relationship between catalyst dosage and dye concentration further explains the role of active site availability and aggregation effects. Fe_3O_4@BC–**1** showed 82.34% degradation for 5 ppm dye using 2 mg of catalyst, but degradation efficiency decreased with higher catalyst dosages and dye concentrations (Fig. 6(d)). Fe_3O_4@BC–**2** reached an optimal degradation efficiency of 83.46% at 5 ppm with 7 mg catalyst, with a decrease at higher concentrations (Fig. 7(d)). Fe_3O_4@BC–**3** in Fig. 8(d) shows robust performance, achieving near-complete degradation (99.61% at 5 ppm and 99.36% at 25 ppm with 12 mg catalyst), suggesting superior dispersion and active site availability.[59]

The effect of catalyst dosage on degradation efficiency varied across different pH levels was also evaluated. For Fe_3O_4@BC–**1** in Fig. 6(e), degradation at pH 9 decreased from 81.68% (2 mg) to 60.09% (12 mg), suggesting that excessive catalyst leads to a decrease in efficiency.[60] Fe_3O_4@BC–**2** showed maximum degradation at pH 9 using 8 mg catalyst (82.31%), while higher dosages (12 mg) led to a slight decline (Fig. 7(e)). Fe_3O_4@BC–**3** exhibited a notable increase in degradation at pH 9, achieving 96.52% efficiency with 12 mg catalyst (Fig. 8(e)). The combined effect of dye concentration and pH further confirmed that alkaline conditions favour degradation. Fe_3O_4@BC–**1** degraded 99.07% of 5 ppm dye at pH 9, but efficiency dropped significantly with higher dye concentrations and acidic pH (Fig. 6(f)). Fe_3O_4@BC–**2** in Fig. 7(f) achieved nearly complete degradation (99.98% at pH 9 with 5 ppm dye), but at 25 ppm, efficiency dropped to 64.83%. Fe_3O_4@BC–**3** followed the same trend, with

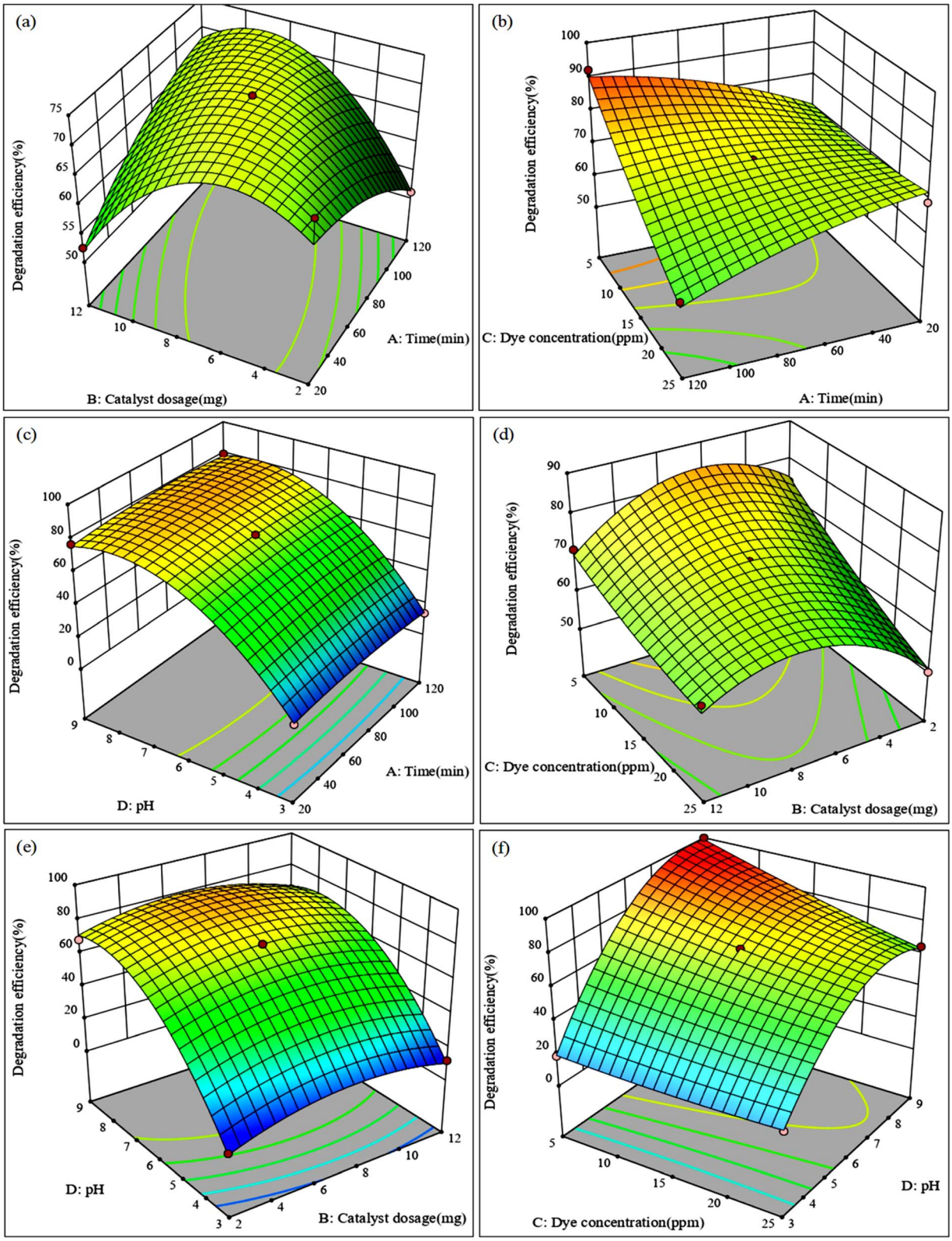

Fig. 7 Degradation of CV by Fe_3O_4@BC−2 3D response surface plots of (a) time *vs.* catalyst dosage, (b) time *vs.* dye concentration, (c) time *vs.* pH, (d) catalyst dosage *vs.* dye concentration, (e) catalyst dosage *vs.* pH and (f) dye concentration *vs.* pH.

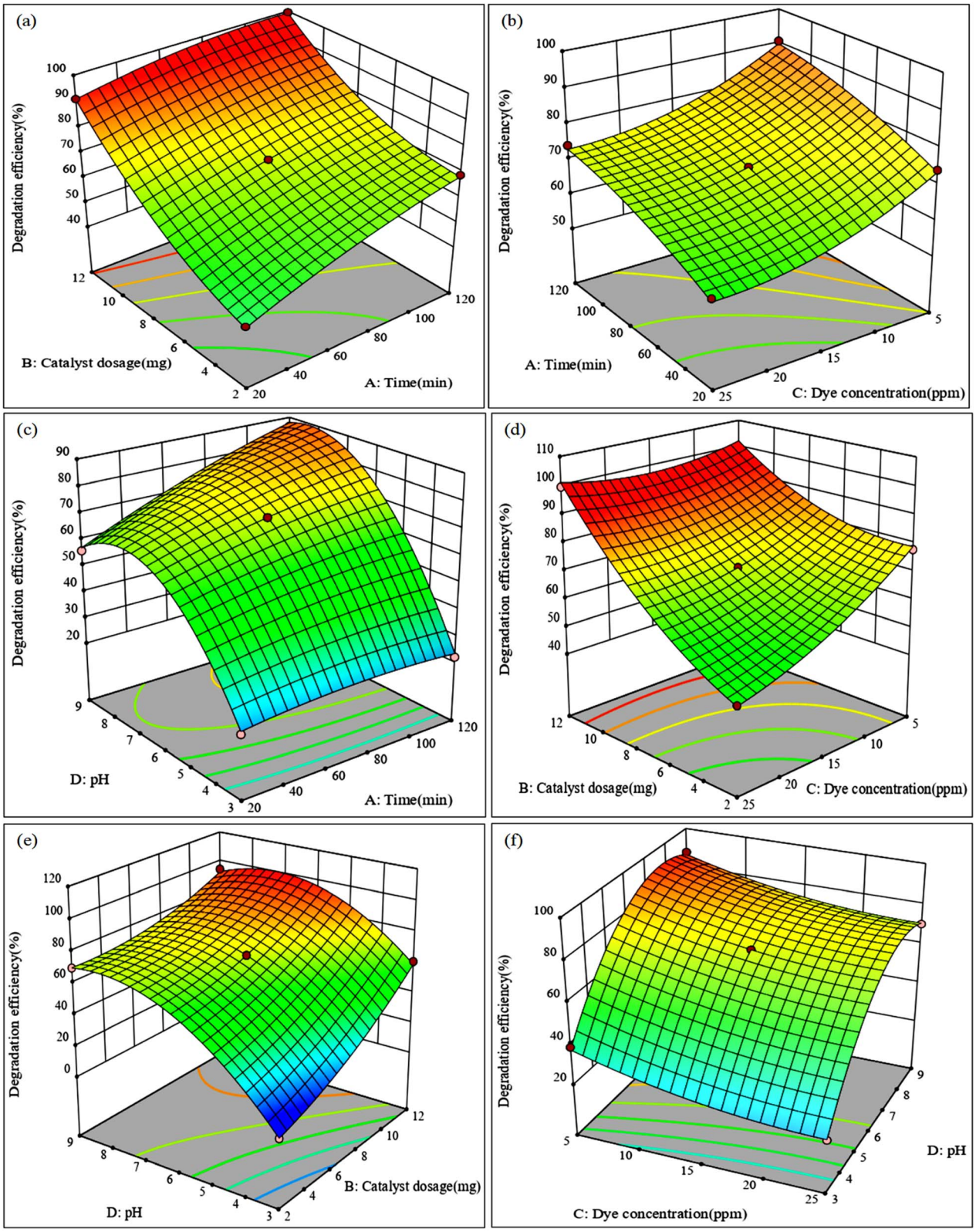

Fig. 8 Degradation of CV by Fe_3O_4@BC–3 3D response surface plots of (a) time *vs.* catalyst dosage, (b) time *vs.* dye concentration, (c) time *vs.* pH, (d) catalyst dosage *vs.* dye concentration, (e) catalyst dosage *vs.* pH and (f) dye concentration *vs.* pH.

Table 2 Predicted optimum conditions for CR and CV degradation by iron oxide nanocomposites

	Time (min)	Catalyst dosage (mg)	Dye concentration (ppm)	pH	Predicted efficiency (%)	Experimental efficiency (%)
CR						
Fe_3O_4@BC–**1**	98	12	20	3	89.04	96.33
Fe_3O_4@BC–**2**	60	4	15	3	96.38	99.42
Fe_3O_4@BC–**3**	120	3	15	3	99.98	99.86
CV						
Fe_3O_4@BC–**1**	60	3	5	9	99.35	96.53
Fe_3O_4@BC–**2**	90	8	5	8	99.98	99.28
Fe_3O_4@BC–**3**	60	2	25	8	99.64	99.10

90.54% degradation at pH 8 using 5 ppm dye, suggesting that alkaline pH enhances catalytic activity (Fig. 8(f)).

4.3 Optimization studies and kinetic analysis of CV and CV degradation using iron oxide nanocomposites

The optimization studies were done following the ramp plots of each catalyst (Fig. S8 and S9). The adjusted optimum conditions are shown in Table 2. Fig. S10 shows UV-vis spectra of the CR and CV dyes degradation. A steady decrease over time indicates the effective degradation of both dyes. An almost flat line at time t suggests near-complete mineralization of the dyes, with minimal residual absorption. High degradation efficiencies ranging between 96.33% and 99.86% were observed for both CR and CV. The narrow bandgap of Fe_3O_4@BC–**2** optimizes light absorption, leading to superior CV degradation.[61] Biochar enhances photocatalytic performance by serving as an electron sink to suppress electron–hole recombination and facilitating charge transfer.[62] The synergistic effect between biochar and iron oxide nanoparticles enhances electron mobility and the photocatalytic efficiency.[63] On the other hand, Fe_3O_4@BC–**3** exhibited high iron content, which enhances CR degradation due to stronger interactions with anionic CR molecules under acidic conditions. Kinetic rate constants indicate that CV degraded faster than CR (Fig. 9 and 10). For CV, k-values are consistently higher (0.05271–0.05926 min^{-1}) than for CR (1.6439×10^{-4}–0.04946 min^{-1}), where Fe_3O_4@BC–**2** exhibited the fastest reaction rate for both dyes. The fast reaction kinetics can be attributed to improved charge separation and reduced recombination, which increases the degradation efficiency.[64] The differences in reaction rates may be attributed to the molecular structures of the dyes and their interaction with the catalyst surface.[65]

To validate the reliability of the RSM optimization, triplicate experiments were conducted under the optimized conditions, and the obtained degradation efficiencies are presented in Table S1. For CR degradation, Fe_3O_4@BC–**3** achieved the highest mean efficiency of 99.86% ± 0.03%, with individual trials at 99.86%, 99.83%, and 99.88%, closely matching the predicted 99.86%. For CV degradation, Fe_3O_4@BC–**2** yielded a mean efficiency of 99.30% ± 0.08%, with trial efficiencies of 99.28%, 99.39%, and 99.24%, which were slightly below the predicted 99.98% but remained highly consistent across the three trials. The low standard deviations across all catalysts indicate good reproducibility, confirming the reliability of the optimized parameters.[66]

4.4 Comparative study

A comparative study was conducted between the Fe_3O_4@BC composites and other reported catalysts for the photocatalytic degradation of CR and CV, as shown in Table 3. Iron oxide based nanomaterials have also been used for the degradation of CV and CR. Jadhav *et al.* synthesized iron oxide nanoparticles *via* the co-precipitation method for the Fenton degradation of 5 ppm crystal violet.[67] Under optimal conditions (pH 7, 5 mg catalyst, and 4 mM H_2O_2), the system achieved a maximum degradation efficiency of 90% within 90 minutes. In another study, iron oxide nanoparticles were synthesized using *Camellia sinensis* leaf extract.[68] The biogenic iron oxide nanoparticles exhibited a mean particle diameter of 49.63 ± 9.23 nm. The removal efficiency of 10 ppm crystal violet was found to be dependent on both concentration and time, achieving a maximum photocatalytic degradation of 99.23% after 210 minutes of sunlight exposure with a catalyst dosage of 1.0 mg mL^{-1}. Cr-doped α-Fe_2O_3 nanoparticles were employed for the enhanced photocatalytic degradation of 30 ppm Congo red dye.[69] A maximum removal efficiency of 95.2% was achieved within 15 minutes of sunlight irradiation using a catalyst dosage of 0.2 g L^{-1} at pH 6. Among the Fe_3O_4@BC composites, Fe_3O_4@BC–**3** achieved a degradation efficiency of 99.86% for CR within 120 minutes, while Fe_3O_4@BC–**2** degraded 99.98% of CV in 90 minutes. These results suggest that the catalysts in the present study outperform the reported catalysts, which require higher catalyst dosages, doping or hydrogen peroxide to degrade the same dyes.

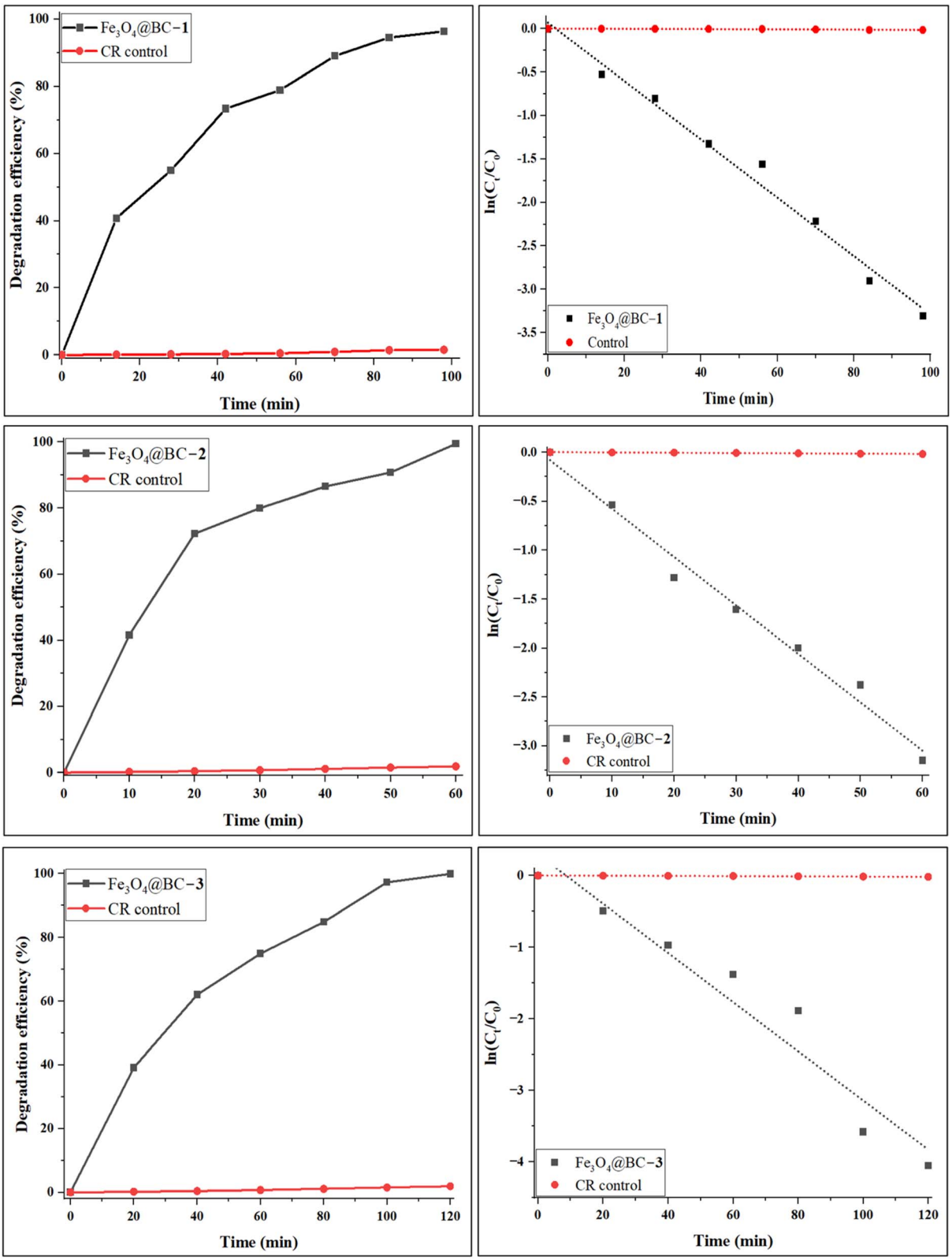

Fig. 9 Congo red photocatalytic degradation efficiency curve and kinetic plots.

4.5 Effect of scavengers

The identification of reactive species involved in the photocatalytic degradation of the dyes is necessary to understand the underlying reaction mechanisms and optimizing the process efficiency. In this study, methanol (MeOH), acrylamide (AC), silver nitrate (SN), and formic acid (FA) were employed as scavengers to quench hydroxyl radicals ($^{\bullet}OH$), superoxide

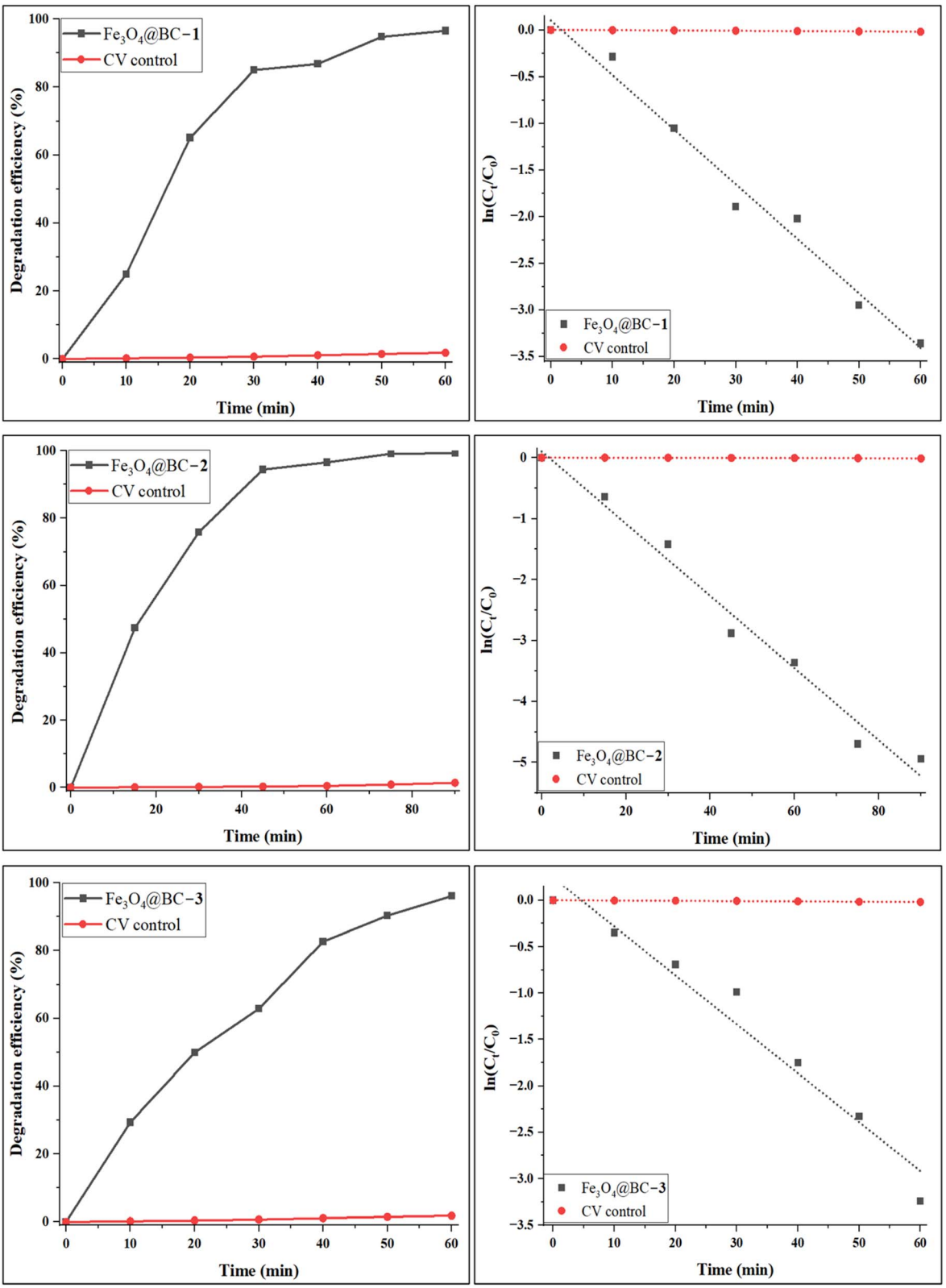

Fig. 10 Crystal violet photocatalytic degradation efficiency curve and kinetic plots.

radicals ($^{\bullet}O_2^-$), electrons (e^-), and photogenerated holes (h^+), respectively. The significant decrease in the degradation efficiency of CV and CR in the presence of these scavengers confirms the involvement of multiple reactive species in the photodegradation process (Fig. S11). Among the scavengers, MeOH exhibited the most pronounced inhibitory effect,

Table 3 The photocatalytic degradation of CR and CV by different nanocomposites

Dye	Catalyst	Light source	Dye concentration (mg L^{-1})	Catalyst dosage (mg)	Time (min)	Degradation efficiency (%)	Ref.
CR	$MnFe_2O_4$/TA/ZnO	Visible	16	50	90	84.2	70
	ZnO-Gd	Visible	10	—	120	68.32	71
	Bs-$CoFe_2O_4$	UV-vis	5	35	90	84	72
	Fe_3O_4@BC–**3**	Visible	15	4	120	99.86	This study
CV	MgO	UV	10	200	130	99.19	73
	Fe-doped TiO_2	Visible	10	30	180	96	74
	Mn-CCMN	UV	13	50	115	98.9	56
	Fe_3O_4@BC–**2**	Visible	5	8	90	99.98	This study

reducing dye degradation from 97.78% to 9.43–23.12%. This suggests that $^{\bullet}OH$ plays a dominant role in the photo degradation mechanism.[75] Hydroxyl radicals are highly reactive species capable of non-selectively oxidizing organic pollutants, and breaks them down into smaller, less toxic intermediates or complete mineralization into CO_2 and H_2O.

Similarly, the addition of AC led to a significant reduction in degradation (10.92–24.88%), indicating that $^{\bullet}O_2^-$ also play a crucial role in the photodegradation process.[76,77] Superoxide radicals are typically generated *via* electron transfer to molecular oxygen and act as secondary oxidizing agents that contribute to dye degradation, either directly or through further conversion into $^{\bullet}OH$.[78] The suppression of degradation in the presence of AC highlights the importance of $^{\bullet}O_2^-$ in sustaining the photocatalytic reaction. The introduction of SN, which acts as an electron scavenger, resulted in a moderate reduction in degradation efficiency (16.92–34.91%). This indicates that photogenerated electrons contribute to the overall reaction by facilitating charge transfer and promoting the formation of reactive oxygen species such as $^{\bullet}O_2^-$ and $^{\bullet}OH$.[79] The lower extent of inhibition compared to MeOH and AC suggests that, while electrons play a supporting role, their impact on degradation is secondary to that of hydroxyl and superoxide radicals. FA, a hole scavenger, caused the least reduction in degradation efficiency (37.64–55.69%), suggesting that photogenerated holes (h^+) are also involved but to a lesser extent than $^{\bullet}OH$ and $^{\bullet}O_2^-$ radicals. Holes typically participate in direct oxidation reactions, either by interacting with the dye molecules or generating $^{\bullet}OH$ from water molecules adsorbed on the catalyst surface.[80] The relatively smaller decline in degradation upon FA addition implies that direct hole-mediated oxidation is not the predominant degradation pathway but still plays a role in overall efficiency.

Based on the scavenger studies results, the possible photocatalytic degradation mechanism for the degradation of CV and CR using the as-prepared Fe_3O_4@BC nanocomposites is illustrated in Scheme 1. Under visible light irradiation, the nanocomposites generate electron–hole pairs as the e^- migrate from the valence band to the conduction band.[81] The photogenerated e^- reduce dissolved oxygen (O_2) to form $^{\bullet}O_2^-$, while h^+ oxidize water molecules to form $^{\bullet}OH$.[82] These radicals oxidize the dye molecules into mineralization products, carbon dioxide and water.[83]

4.6 Photostability of the iron oxide nanocomposites

The graphs in Fig. S12 illustrate the recyclability of the three catalysts (Fe_3O_4@BC, Fe_3O_4@BC–**2**, and Fe_3O_4@BC–**3**) used for the degradation of CR and CV over six successive cycles. All

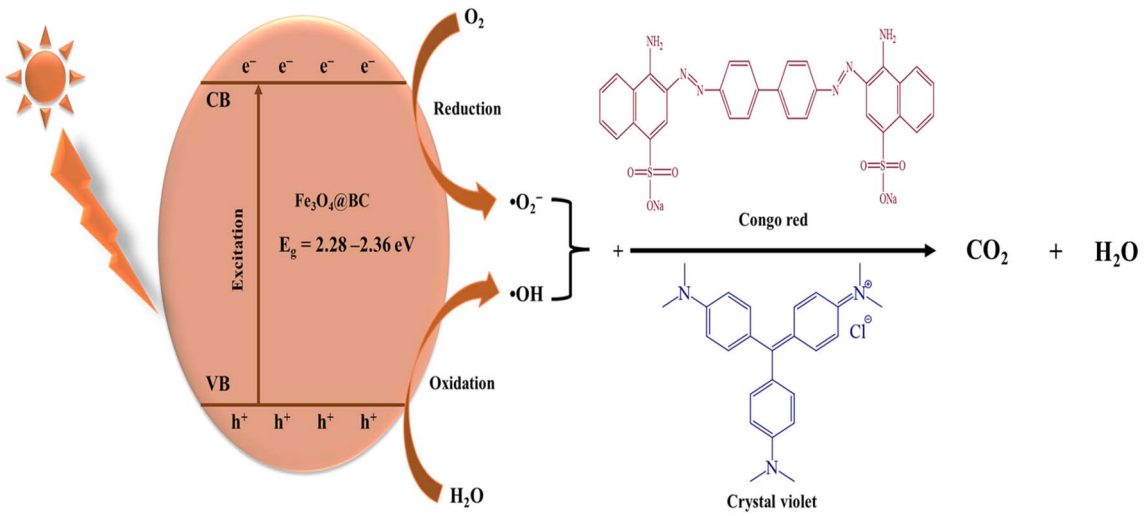

Scheme 1 Proposed photocatalytic degradation pathway.

three catalysts exhibit a progressive decrease in degradation efficiency over successive cycles. Fe_3O_4@BC–**2** maintains relatively high degradation efficiency for the first two cycles but sharply declines after the third cycle over CV. Fe_3O_4@BC–**1** and Fe_3O_4@BC–**3** demonstrate good recyclability, maintaining relatively high photodegradation efficiency over CR but with a noticeable decrease on the fifth cycle. The recyclability trends suggest some level of catalyst deactivation, which may be due to the adsorption of degradation by products onto the catalyst surface, blocking active sites.[84]

5. Conclusion

Iron oxide nanocomposites were synthesized using an ultrasound-assisted method with varying ultrasonic irradiation time to investigate the influence of time on their morphological, optical, and photocatalytic properties. TEM analysis revealed different morphologies for the nanocomposites: Fe_3O_4@BC–**1** exhibited irregular rod- and plate-like structures with an average diameter of 6.4 nm, Fe_3O_4@BC–**2** displayed square-shaped particles with a mean size of 8.3 nm, and Fe_3O_4@BC–**3** consisted of agglomerated, irregularly shaped particles averaging 9.8 nm in size. These findings demonstrate that increasing sonication time significantly affects the particle size and shape of the iron oxide nanocomposites. The bandgap energies were determined to be 2.36 eV, 2.28 eV, and 2.32 eV for Fe_3O_4@BC–**1**, Fe_3O_4@BC–**2**, and Fe_3O_4@BC–**3**, respectively. The nanocomposites were evaluated as photocatalysts for the degradation of CR and CV using response surface methodology. Fe_3O_4@BC–**2** achieved the highest degradation of CV (99.98% in 90 minutes under optimized conditions: 8 mg catalyst, 5 ppm dye, pH 8), while Fe_3O_4@BC–**3** exhibited superior activity for CR (99.86% in 120 minutes, 3 mg catalyst, 15 ppm dye, pH 3). Among the nanocomposites, Fe_3O_4@BC–**2** exhibited faster degradation rates for both dyes. The high degradation efficiencies demonstrate the importance of optimizing the reaction parameters to maximize photocatalytic activity, providing a model for efficient and scalable wastewater treatment. Scavenger studies were conducted to elucidate the photocatalytic mechanism, revealing that $^{\bullet}OH$ plays a dominant role, with $^{\bullet}O_2^-$ playing a significant secondary role in the degradation of CR and CV. Additionally, the as-prepared nanocomposites demonstrated excellent photostability and recyclability, making them promising candidates for the photocatalytic degradation of organic dyes. However, the potential for iron leaching from the nanocomposites into the treated water was not investigated in this study, which is a critical factor for assessing long-term environmental safety and catalyst stability. Future work should include quantitative analysis of iron leaching to ensure the nanocomposites meet environmental safety standards. By advancing efficient photocatalytic technologies for water purification and utilizing biochar from agricultural biomass, this work supports SDG 6 (Clean Water and Sanitation) by contributing to target 6.3 for improved water quality through pollution reduction, SDG 12 (Responsible Consumption and Production) by promoting biomass waste reuse under target 12.5, and SDG 13 (Climate Action) by fostering sustainable technologies that mitigate pollution-related environmental impacts under target 13.3.

Conflicts of interest

The authors declare no conflicts of interest.

Data availability

All relevant data have been included in the manuscript or as supplementary information (SI). Supplementary information: preparation of *Portulacaria afra* biochar (Scheme S1); p-XRD pattern of biochar (Fig. S1); size distributions of iron oxide nanocomposites prepared at different ultrasound irradiation times (Fig. S2); SEM images and EDX spectra of Fe_3O_4@BC nanocomposites (Fig. S3); FTIR spectra of magnetite nanoparticles; biochar and Fe_3O_4@BC nanocomposites before (A) and after (B) photocatalysis (Fig. S4); UV-Vis spectra and Tauc plots of iron oxide nanocomposites (Fig. S5); predicted *versus* actual degradation of CV and CR (Fig. S6); perturbation plots showing the effect of the independent variables on CV dye and CR degradation (Fig. S7); ramp plot showing numerical optimization for CV degradation (Fig. S8); ramp plot showing numerical optimization for CR degradation (Fig. S9); absorption spectra of Congo red (CR) and crystal violet (CV) dyes degradation by iron oxide nanocomposites (Fig. S10); Congo red photocatalytic degradation efficiency curve and kinetic plots (Fig. S11); crystal violet photocatalytic degradation efficiency curve and kinetic plots (Fig. S12); effect of scavengers on the degradation of Congo red and crystal violet dye by iron oxide nanocomposites (Fig. S13); recyclability of Fe_3O_4@BC nanocomposites over CV and CR dyes (Fig. S14); degradation efficiencies from triplicate trials under optimized conditions (Table S1); experimental design matrix and response results for Congo red (CR) and crystal violet (CV) by Fe_3O_4@BC–**1** (Table S2); experimental design matrix and response results for Congo red (CR) and crystal violet (CV) by Fe_3O_4@BC–**2** (Table S3); experimental design matrix and response results for Congo red (CR) and crystal violet (CV) by Fe_3O_4@BC–**3** (Table S4); analysis of variance (ANOVA) for CR degradation using Fe_3O_4@BC–**1** composite (Table S5); analysis of variance (ANOVA) for CR degradation using Fe_3O_4@BC–**2** composite (Table S6); analysis of variance (ANOVA) for CR degradation using Fe_3O_4@BC–**3** composite (Table S7); analysis of variance (ANOVA) for CV degradation using Fe_3O_4@BC–**1** composite (Table S8); analysis of variance (ANOVA) for CV degradation using Fe_3O_4@BC–**2** composite (Table S9); analysis of variance (ANOVA) for CV degradation using Fe_3O_4@BC–**3** composite (Table S10). See DOI: https://doi.org/10.1039/d5ra09734g.

Acknowledgements

The authors acknowledge financial support from the National Research Foundation (NRF), South Africa through competitive funding for rated researchers (Grant Number: CPRR23042396404), Thandi Mbuyazi acknowledge the award of NRF PhD scholarship.

References

1 B. J. Singh, A. Chakraborty and R. Sehgal, *J. Environ. Manage.*, 2023, **348**, 119230.
2 A. P. Periyasamy, *Sustainability*, 2024, **16**, 495.
3 S. Dutta, S. Adhikary, S. Bhattacharya, D. Roy, S. Chatterjee, A. Chakraborty, D. Banerjee, A. Ganguly, S. Nanda and P. Rajak, *J. Environ. Manage.*, 2024, **353**, 120103.
4 K. Z. Elwakeel, A. M. Elgarahy, G. A. Elshoubaky and S. H. Mohammad, *J. Environ. Health Sci. Eng.*, 2020, **18**, 35–50.
5 M. Akdemir, B. Isik, F. Cakar and O. Cankurtaran, *Mater. Chem. Phys.*, 2022, **291**, 126763.
6 N. Kuppan, M. Padman, M. Mahadeva, S. Srinivasan and R. Devarajan, *Waste Manag. Bull.*, 2024, **2**, 154–171.
7 P. Sarojini, K. Leeladevi, T. Kavitha, K. Gurushankar, G. Sriram, T. H. Oh and K. Kannan, *Materials*, 2023, **16**, 5800.
8 S. S. Emmanuel, A. A. Adesibikan, C. O. Olawoyin and M. O. Idris, *ChemistrySelect*, 2024, **9**, e202400316.
9 Z. Zheng, J. He, Z. Zhang, A. Kumar, M. Khan, C. W. Lung and I. M. C. Lo, *Environ. Sci. Nano*, 2024, **11**, 1784–1816.
10 K. Kannan, D. Radhika, D. Gnanasangeetha, S. K. Lakkaboyana, K. K. Sadasivuni, K. Gurushankar and M. M. Hanafiah, *Inorg. Chem. Commun.*, 2021, **125**, 108429.
11 S. Liu, B. Yu, S. Wang, Y. Shen and H. Cong, *Adv. Colloid Interface Sci.*, 2020, **281**, 102165.
12 H. Dhila, A. Bhapkar and S. Bhame, *Desalin. Water Treat.*, 2025, **321**, 101004.
13 E. Amdeha, *Biomass Convers. Biorefin.*, 2023, **14**, 23293–23318.
14 M. M. Gaber, H. Shokry, M. Samy and E. A. El-Bestawy, *Chemosphere*, 2024, **364**, 143245.
15 R. Ma, Y. Sun, H. Zhang, J. Zhu, H. Tian, X. Guo, R. Wang, X. Cui, X. Hou and S. An, *RSC Adv.*, 2024, **14**, 19707–19717.
16 V. Gadore, A. K. Singh, S. R. Mishra and M. Ahmaruzzaman, *Sci. Rep.*, 2024, **14**, 1118.
17 S. Ben Moussa, *J. Photochem. Photobiol.*, 2024, **447**, 115284.
18 T. Hai, R. Chaturvedi, L. Mostafa, T. I. Kh, N. F. Soliman and W. El-Shafai, *J. Phys. Chem. Solids*, 2024, **185**, 111747.
19 A. R. Dash, A. J. Lakhani, D. Devi Priya, T. V. Surendra, M. M. R. Khan, E. J. J. Samuel and S. M. Roopan, *J. Cluster Sci.*, 2023, **34**, 121–133.
20 T. B. Mbuyazi and P. A. Ajibade, *RSC Adv.*, 2025, **15**, 6400–6412.
21 K. Sathya, R. Saravanathamizhan and G. Baskar, *Ultrason. Sonochem.*, 2017, **39**, 446–451.
22 S. Afshin, Y. Rashtbari, M. Vosough, A. Dargahi, M. Fazlzadeh, A. Behzad and M. Yousefi, *J. Water Process Eng.*, 2021, **42**, 102113.
23 K. Ramesh and V. Raghavan, *ACS Omega*, 2024, **9**, 4377–4385.
24 N. Divyangkumar and N. L. Panwar, *Energy 360*, 2025, **3**, 100014.
25 T. Shen, Y. Inagaki, M. Komori and Y. Sakakibara, *J. Water Process Eng.*, 2022, **48**, 102817.
26 E. J. Lukhele, J. T. Khutlane, N. B. Báthori and R. Malgas-Enus, *Surf. Interfaces*, 2022, **31**, 101970.
27 R. Kumar, V. B. Kumar and A. Gedanken, *Ultrason. Sonochem.*, 2020, **64**, 105009.
28 C. Devos, A. Bampouli, E. Brozzi, G. D. Stefanidis, M. Dusselier, T. Van Gerven and S. Kuhn, *Chem. Soc. Rev.*, 2025, **54**, 85–115.
29 Y. Hadadian, H. Masoomi, A. Dinari, C. Ryu, S. Hwang, S. Kim, B. k. Cho, J. Y. Lee and J. Yoon, *ACS Omega*, 2022, **7**, 15996–16012.
30 M. D. Noviastuti, E. K. Sari, A. Jiananda, N. Imani Istiqomah, L. J. Mahardhika, D. A. Larasati, Sudarmono, J. Angel, A. D. Nugraheni and E. Suharyadi, *Results Chem.*, 2025, **16**, 102495.
31 J.-H. Yang, C.-P. Wang, B.-H. Chen and M. H. Huang, *Inorg. Chem.*, 2025, **64**, 8659–8667.
32 D. Egea-Benavente, C. Díaz-Ufano, A. Gallo-Cordova, F. Palomares, J. Lehman, C. Huaman, D. Barber, M. Del, M. d. P. Morales, B. Jeyadevan and N. H. Csic, *ACS Appl. Mater. Interfaces*, 2023, **15**, 32162–32176.
33 P. Soltanpour, R. Naderali and K. Mabhouti, *Sci. Rep.*, 2024, **14**, 21287.
34 G. Jajko-Liberka, M. G. Anagha, P. Chytrosz-Wróbel, P. Kubisiak, W. Kulig, L. Cwiklik and A. Kotarba, *Ultrason. Sonochem.*, 2025, **121**, 107559.
35 L. I. Ledesma-Fosados, N. V. Gallardo-Rivas, U. Páramo-García, R. García-Alamilla, J. d. J. Pérez-Bueno and A. M. Mendoza-Martínez, *Int. J. Electrochem. Sci.*, 2025, **20**, 100956.
36 B. Lesiak, N. Rangam, P. Jiricek, I. Gordeev, J. Tóth, L. Kövér, M. Mohai and P. Borowicz, *Front. Chem.*, 2019, **7**, 642.
37 Y. Mhosva, P. Nkomozepi, S. Nalla and T. Nyakudya, *Sci. Afr.*, 2024, **26**, e02491.
38 J. M. Tharayil, P. Chinnaiyan, B. Ramasamy and A. Sathasivan, *Environ. Technol. Innov.*, 2025, **39**, 104337.
39 T. K. Alshammari, S. K. Ghoshal, H. Bakhtiar, A. A. Salim and S. S. Alias, *Mater. Chem. Phys.*, 2024, **318**, 129235.
40 D. Khadka, P. Gautam, R. Dahal, M. D. Ashie, H. Paudyal, K. N. Ghimire, B. Pant, B. R. Poudel, B. P. Bastakoti and M. R. Pokhrel, *Catalysts*, 2024, **14**, 751.
41 P. Makuła, M. Pacia and W. Macyk, *J. Phys. Chem. Lett.*, 2018, **9**, 6814–6817.
42 Q. Li, K. Wu, H. Zhu, Y. Yang, S. He and T. Lian, *Chem. Rev.*, 2024, **124**, 5695–5763.
43 T. Qiao and D. H. Son, *Acc. Chem. Res.*, 2021, **54**, 1399–1408.
44 M. U. Sajid and Y. Bicer, *Ultrason. Sonochem.*, 2022, **88**, 106079.
45 E. Bazrafshan, L. Mohammadi, A. A. Zarei, J. Mosafer, M. N. Zafar and A. Dargahi, *RSC Adv.*, 2023, **13**, 25408–25424.
46 Q. Zaib, M. Jouiad and F. Ahmad, *ACS Omega*, 2019, **4**, 535–545.
47 S. N. Tan, M. L. Yuen and R. A. Ramli, *Green Anal. Chem.*, 2025, **12**, 100230.
48 M. Abul Bashar, A. B. M. Ibrahim, M. K. Hasan and M. S. Hossain, *RSC Adv.*, 2025, **15**, 41710–41723.
49 M. R. Ardani, A. L. Pang, U. Pal, M. A. S. M. Haniff, A. G. Ismail, A. A. Hamzah, W. A. Khanday and M. Ahmadipour, *Diam. Relat. Mater.*, 2023, **137**, 110066.

50 S. Zahoor, S. Muhammad, M. Kashif, N. Shahzad, Y.-c. Liu, C. Celik, N. Ambreen, A. Ali, H.-F. Wu, S. Azizi and C. Wen, *Coord. Chem. Rev.*, 2026, **549**, 217239.
51 J. Cao, H. Zhou, C. Huang, Q. Wu and W. Yao, *J. Colloid Interface Sci.*, 2023, **645**, 794–805.
52 A. Bhuyan and M. Ahmaruzzaman, *J. Alloys Compd.*, 2024, **972**, 172781.
53 M. Alsawat, *Int. J. Electrochem. Sci.*, 2024, **19**, 100611.
54 K. Yoshida, *J. Chem.*, 2024, **3**, 12–20.
55 R. Mohammadzadeh Kakhki and H. Bolandhemmat, *Sci. Rep.*, 2024, **14**, 19009.
56 Y. Yang, H. Khan, S. Gao, A. K. Khalil, N. Ali, A. Khan, P. L. Show, M. Bilal and H. Khan, *Chemosphere*, 2022, **306**, 135647.
57 M. Zahmatkesh Anbarani, S. Nourbakhsh, A. Toolabi and Z. Bonyadi, *Heliyon*, 2023, **9**, e19460.
58 Y. Wang, Q. Geng, J. Yang, Y. Liu and C. Liu, *ACS Omega*, 2020, **5**, 31137–31145.
59 A. Mohammadpour, A. Kazemi, M. A. Baghapour, M. R. Samaei, K. Kannan and A. Mousavi Khaneghah, *Int. J. Biol. Macromol.*, 2024, **277**, 134060.
60 M. F. Sanakousar, C. C. Vidyasagar, V. M. Jiménez-Pérez, B. K. Jayanna, Mounesh, A. H. Shridhar and K. Prakash, *J. Hazard. Mater. Adv.*, 2021, **2**, 100004.
61 S. Nachimuthu, C. Thangamani, N. Thiyagarajulu, K. Thangaraj, D. Paramasivam, S. Thangavel, K. Kannan, C. Parvathiraja, V. B. Visalakshi, P. Velmurugan, A. Chinnathambi, S. A. Alharbi and N. Basavegowda, *Catal. Commun.*, 2023, **184**, 106786.
62 D. Feng, J. Lü, S. Guo and J. Li, *J. Environ. Chem. Eng.*, 2021, **9**, 104677.
63 S. Cheng, S. Zhao, B. Xing, Y. Liu, C. Zhang and H. Xia, *J. Clean. Prod.*, 2022, **348**, 131301.
64 M. Sultana and M. Ahmaruzzaman, *Environ. Sci. Pollut. Res.*, 2023, **30**, 83463–83484.
65 M. Hachemaoui, B. Boukoussa, I. Ismail, A. Mokhtar, I. Taha, J. Iqbal, S. Hacini, A. Bengueddach and R. Hamacha, *Colloids Surf., A*, 2021, **623**, 126729.
66 N. Vaz, J. Choi, S. Kim and H. Ju, *Energy Convers. Manage.*, 2024, **322**, 119183.
67 A. Jadhav, R. Chavan, S. Sonawane, P. Kamble, S. Mahajan, R. Ghorpade, A. Chougale, N. Abd El-Salam, H. Fouad and R. Patil, *J. Nanoelectron. Optoelectron.*, 2024, **19**, 272–277.
68 M. T. Yassin, F. O. Al-Otibi and A. A. Al-Askar, *Separations*, 2023, **10**, 513.
69 P. Yadav, N. Dhariwal, M. Kumari, V. Kumar and O. P. Thakur, *Chemosphere*, 2023, **343**, 140208.
70 B. Boutra, N. Güy, M. Özacar and M. Trari, *J. Magn. Magn. Mater.*, 2020, **497**, 165994.
71 A. Sadek Kadari, Y. Khane, A. Nebatti Ech-Chergui, A. Popa, M. h. Guezzoul, D. Silipas, F. Bennabi, A. Zoukel, E. Akyildiz, K. Driss-Khodja and B. Amrani, *Inorg. Chem. Commun.*, 2022, **142**, 109626.
72 N. Ali, A. Said, F. Ali, F. Raziq, Z. Ali, M. Bilal, L. Reinert, T. Begum and H. M. N. Iqbal, *Water, Air, Soil Pollut.*, 2020, **231**, 50.
73 S. E. A. Elashery, I. Ibrahim, H. Gomaa, M. M. El-Bouraie, I. A. Moneam, S. S. Fekry and G. G. Mohamed, *Magnetochemistry*, 2023, **9**, 56.
74 A. Mancuso, N. Blangetti, O. Sacco, F. S. Freyria, B. Bonelli, S. Esposito, D. Sannino and V. Vaiano, *Nanomaterials*, 2023, **13**, 270.
75 Z. H. Jabbar, A. A. Okab, B. H. Graimed, M. A. Issa and S. H. Ammar, *Diam. Relat. Mater.*, 2023, **133**, 109711.
76 H. Zhou, Y. Qiu, C. Yang, J. Zang, Z. Song, T. Yang, J. Li, Y. Fan, F. Dang and W. Wang, *Molecules*, 2022, **27**, 8642.
77 M. Saeed, R. D. Pecho, S. Panchal, S. K. Alhag, L. A. Al-Shuraym, K. M. Al Syaad and U. H. Bhutta, *Water*, 2023, **15**, 2840.
78 Z. Bi, W. Wang, L. Zhao, X. Wang, D. Xing, Y. Zhou, D.-J. Lee, N. Ren and C. Chen, *Environ. Res.*, 2024, **260**, 119592.
79 G. Rangarajan, A. Jayaseelan and R. Farnood, *J. Clean. Prod.*, 2022, **346**, 131155.
80 S. S. Bag, S. Sinha, A. Banerjee and A. Golder, *J. Environ. Chem. Eng.*, 2022, **10**, 108919.
81 S. S. Emmanuel, M. O. Idris, C. O. Olawoyin, A. A. Adesibikan, A. A. Aliyu and A. I. Suleiman, *ChemistrySelect*, 2024, **9**, e202304956.
82 H. Saraee, Z. Noorimotlagh, M. Mansouri, S. A. Mirzaee and S. S. Martinez, *Environ. Technol.*, 2024, **45**, 4359–4375.
83 S. S. Emmanuel, A. A. Adesibikan, S. M. Tichapondwa, M. P. Rayaroth, F. Bosca, M. L. Marin, B. A. Samejo and G. Boczkaj, *Sustainable Mater. Technol.*, 2025, e01683.
84 Y. Huang, J. Xu, H. Ling, W. Liu and F. Jiao, *Langmuir*, 2024, **40**, 26371–26386.